

Plagioclase under compression: A path to diaplectic glass and maskelynite

Tianqi Xie^{1,2*}, Sean R. Shieh^{1*}, Stella Chariton³, Mauritz van Zyl¹, Ricardo D. Rodriguez¹, Vitali B. Prakapenka³, Dongzhou Zhang³

Diaplectic glass and maskelynite in shocked plagioclase serve as key diagnostic features for high level of shock metamorphism in impact craters and meteorites. However, their formation mechanisms remain unclear and have long been argued, mainly due to the lack of phase diagram for plagioclase with extended pressure-temperature conditions. We report the stabilities of labradorite and anorthite at pressure up to 65 gigapascals and temperature up to 4000 kelvin. Our experimental results reveal the pressure-temperature conditions for amorphization, decomposition, and melting of labradorite and anorthite. The boundary between amorphous plagioclase and crystalline high-pressure phases in our phase diagram indicate diaplectic glass can form at 1300 to 1500 kelvin, and the melting line suggests that maskelynite can be generated above 3000 kelvin at high pressures. Formation conditions of diaplectic glass and maskelynite in plagioclase-bearing rocks are also suggested by the combination of phase diagram and shock Hugoniot data. These findings will advance our understanding of the bombardment history on rocky planetary surfaces.

Copyright © 2025 The Authors, some rights reserved; exclusive licensee American Association for the Advancement of Science. No claim to original U.S. Government Works. Distributed under a Creative Commons Attribution NonCommercial License 4.0 (CC BY-NC).

INTRODUCTION

Plagioclase feldspar is the most abundant component of igneous rocks in Earth's crust and commonly appears as a solid solution, ranging from anorthite ($\text{CaAl}_2\text{Si}_2\text{O}_8$) to albite ($\text{NaAlSi}_3\text{O}_8$) in composition. Plagioclase is also found on the other rocky planetary bodies throughout our solar system. Anorthite is widely found on the highland of the Moon, and intermediate plagioclase has been detected remotely on the surface of Mars, Venus, and Mercury (1–7). When the surfaces of these rocky bodies got bombarded by hyper-velocity impactors, plagioclase would be subjected to high pressure and heat from the shock wave (8–10). The microscopic features, preserved in terrestrial impact structures and meteorites, are key in characterizing the impact events. Among the variety of shock features observed in plagioclase-rich rocks, diaplectic glass and maskelynite are regarded as the most diagnostic ones for high level shock metamorphism (8, 11, 12).

Diaplectic glass was first observed in the Ries impact structure and named by von Englehardt in 1967. The word "diaplectic" was derived from the Greek word *diaplesso*, which means to destroy by striking (13, 14). Diaplectic glass refers to the colorless, optically isotropic grains that retain the chemical composition, morphology, and inherited texture of the original plagioclase crystals. It has been observed in terrestrial impact structures with intermediate plagioclase composition (9, 15, 16), and fewer cases have been reported with anorthite composition ($\text{An}_{73–96}$) from lunar samples returned by the Apollo missions (17, 18). Unlike fused glass, no flow textures or vesicles are observed in diaplectic glass, suggesting that it is formed by a solid-state transformation. Reproduced experimentally, diaplectic glass has been observed in the quench product of dynamic shock experiments on plagioclase and plagioclase-rich rocks (19–26), and its pressure-induced amorphous nature has been proved by

compressing plagioclase under static high-pressure conditions (27–30). The current classification system for progressive shock metamorphism outlines the pressure range of 28 to 45 GPa for the formation of diaplectic glass in plagioclase-rich rocks (12), but the formation temperature range remains uncertain due to the difficulty of temperature measurement in dynamic experiments.

Maskelynite was originally observed in the Shergotty Martian meteorite and named by G. Tschermak in 1872 in honor of Mervyn Herbert Nevil Story-Maskelyne. Initially, he described it as a new cubic mineral with a composition similar as labradorite from Labrador, Canada but later reinterpreted it as a pseudomorphs product formed from labradorite via melting (31–33). Since then, maskelynite has been observed in ordinary chondrites, Lunar, Vestian, and Martian meteorites (11). Maskelynite is colorless and optically isotropic similar to diaplectic glass, but it lacks textures such as inherited fractures, cleavages from plagioclase and shock-induced fractures. Bordered by surrounding crystals, maskelynite generally displays a nonvesicular flow pattern. Surrounding minerals usually show radiated fractures emerging from the smooth maskelynite, which may result from volume expansion during the melting of plagioclase and shrinkage from solidification (8, 34, 35). However, the melting point of plagioclase was mostly studied at low pressures, and the melting point at high pressure was very limited (36–40), leading to ambiguity when interpreting the formation of maskelynite and melt veins within meteorites.

Now, when describing isotropic grains with plagioclase composition observed from terrestrial impact structures or meteorites, the names of "diaplectic glass" and "maskelynite" have been used interchangeably, but with controversial interpretations on their formation conditions. This could be largely due to the lack of understanding of the behavior of plagioclase under high pressures and temperatures. Phase diagrams of end-member plagioclase felspar are only reported at pressure ranges up to 25 GPa and temperature up to 2500 K (41–44), much lower than the corresponding pressure-temperature range of high-level shock stages expected from hyper-velocity impact events. There is no phase diagram of intermediate plagioclase available.

¹Department of Earth Sciences, University of Western Ontario, London, ON N6K 5B7, Canada. ²Geological Sciences, University of Saskatchewan, Saskatoon, SK S7N 5E2, Canada. ³Center for Advanced Radiation Sources, The University of Chicago, Chicago, IL 60637, USA.

*Corresponding author. Email: t.xie@uwo.ca (T.X.); sshieh@uwo.ca (S.R.S.)

RESULTS AND DISCUSSION

Decomposition of plagioclase

To understand the stability of plagioclase, we conducted *in situ* high-pressure and high-temperature x-ray diffraction measurements on intermediate plagioclase labradorite (An_{51}) and anorthite (An_{96}) (detailed chemical compositions listed in table S1) at pressure up to 65 GPa and 4000 K. Phase assemblages were identified during prolonged high-pressure–temperature experiments and from mapping the heated spots in quenched samples at room temperature and high pressures. Representative diffraction patterns of the phase assemblages under different pressures at room temperature are shown in Figs. 1 to 3, and the parameters for these phases are shown in table S2.

During *in situ* high pressure-temperature experiments, labradorite (An_{51}) decomposed into jadeite (Jd) + stishovite (St) + Ca-Al silicate (CAS) + grossular (Gr) at pressure around 15 GPa and temperature higher than 1300 K. At 23 to 27 GPa and temperature above 1300 K, the phase assemblage transformed to St + CAS + $CaSiO_3$ perovskite (Dvm) + $CaFe_2O_4$ -type (CF) phase + corundum (Crn). At 28 to 50 GPa and temperature above 1400 K, a phase assemblage of St + Dvm + CF + Crn was observed initially, and then St + Dvm + Crn + new phase was observed at higher pressure-temperature conditions. The new phase was found emerging above 43 GPa and >1500 K. The most intense peaks of this new phase were seen right next to intense Dvm peak near 8°, and right next to Pt peak near 9°, the diffraction rings belonging to the new phase can be identified by their spotted feature (Fig. 2B). Using GSASII and Crysfire2020, the new phase obtained at 60 GPa (Fig. 2) was tentatively assigned to a tetragonal crystal structure with $a = 3.3832$ (3) Å, $b = 3.3832$ (3) Å, $c = 4.7307$ (8) Å, $\alpha = \beta = \gamma = 90^\circ$. Compared with calculated patterns by Powdercell software using these parameters, this new phase has a space group no higher than P4/mmm.

Several samples were later decompressed to 1 bar, and quenchable phases were identified by x-ray diffraction mapping. We found several phases i.e., Jd, St, CAS, Gr, and Crn can be retained at ambient conditions but not all. The new phase was not seen in the recovered sample, nor was Dvm or CF phase. Element mapping of the quenched sample was also performed to help identify phases with element enrichments (fig. S1). It seems that most of the elements are relatively even distributed. However, Al shows slightly concentrated at particular spots which can be assigned to the Al_2O_3 (Crn) phases. A few spots with high Ca concentration were also observed and seem to show free or low Al, Na and K concentration. Furthermore, a close look at the triangle grain in fig. S1 confirms it to be Ca-Pv ($CaSiO_3$) in composition. Na and K did not appear to mix with each other and may form separate Na-bearing (e.g., Jd or CF) and K-bearing high-pressure phases. Note that the concentration of K in our samples is too low to be confidently attributed to any phase, but K-bearing phases might contribute to some unidentified peaks in Figs. 1 and 3.

Similar to labradorite but lacking Na-rich phase, anorthite (An_{96}) decomposed to St + kyanite (Ky) + Gr above 12 GPa and >1300 K. Next, this phase assemblage transformed into St + CAS + Gr at 15 to 22 GPa with temperature above 1600 K, St + CAS + Dvm at 22 to 27 GPa and temperature above 1700 K and then St + Dvm + Crn at >27 GPa and $T > 1700$ K. No new phase was found from this composition at pressure above 42 GPa. When quenched from above 27 GPa, St and Crn were the two crystalline phases observed from the quenched product, while Dvm phase became amorphous at ambient conditions.

Phase diagram of labradorite and anorthite

Based on our observation from *in situ* x-ray diffraction data, we were able to draw pressure-temperature boundaries between amorphization

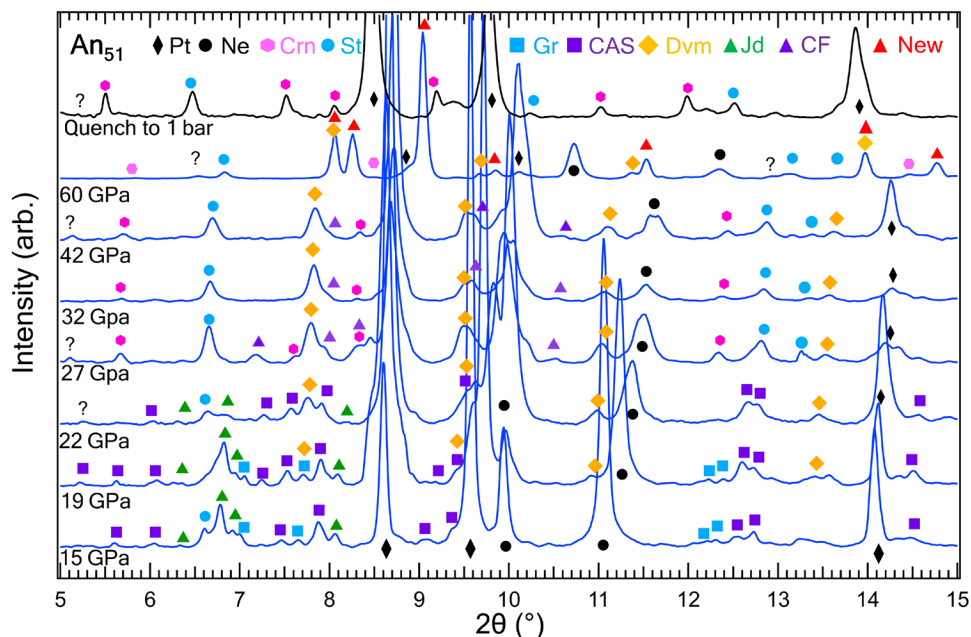


Fig. 1. High-pressure phase assemblages from decomposition of labradorite. Representative XRD patterns of labradorite An_{51} obtained at 15 to 60 GPa after quenching from high temperatures. Only Crn and St were observed in quenched samples obtained from 60 GPa. Different solid symbols denote different phases. Pt, Platinum; Ne, Neon; Jd, Jadeite; St, Stishovite; CAS, Ca-Al silicate; Gr, Grossular; Dvm, $CaSiO_3$ perovskite; CF, $CaFe_2O_4$ -type (CF) phase; Crn, Corundum; New, new phase.

and decomposition of plagioclase and were also able to draw the melting line. Building upon previously reported phase relations (29, 41–47), we construct a phase diagram for labradorite and update the phase diagram of anorthite with extended pressure-temperature range, as in Fig. 4.

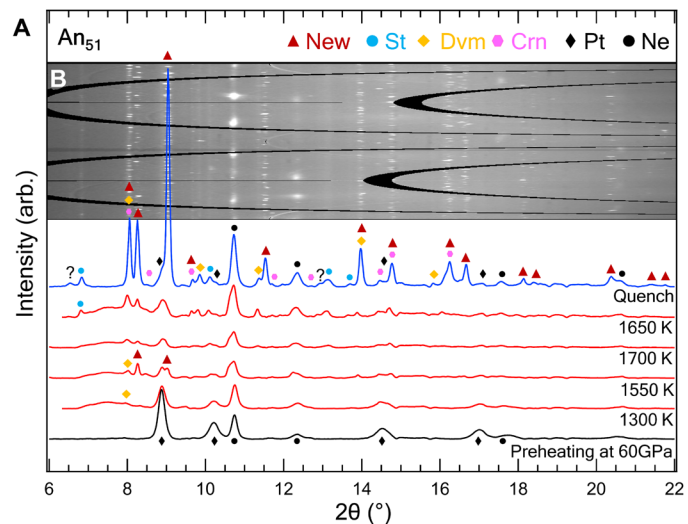


Fig. 2. Synthesis of the new phase. (A) Diffraction patterns obtained from different temperatures at 60 GPa. Different colored symbols denote different phases. (B) Cake image of the diffraction pattern obtained from 60 GPa after temperature quench.

We observed the amorphization of labradorite above 22 GPa and temperature < 1200 K, in agreement with the crystalline to amorphization boundary reported by Kubo *et al.* (29) (Fig. 4A). The complete amorphization was identified by the loss of all Raman peaks at room temperature and x-ray diffraction patterns during heating, suggesting the vanish of crystallinity (fig. S2). Upon heating from amorphization, we observed the emerging of new peaks, and we were thus able to draw the moderate-temperature boundary around 1200 K between amorphous and high-pressure phases. The boundary between Jd + St + CAS + Gr and CF + St + CAS + Dvm + Cr was mainly determined by the disappearance of Jd and appearance of CF. When compressed above 22 GPa and >1400 K, no Jd was observed, while the CF phase was still observable but weak. This pressure-temperature range agrees well with the previous reports (29, 41, 43, 48). The boundary between CF + St + CAS + Dvm + Cr and CF + St + Dvm + Cr was determined mainly due to the disappearance of CAS phase. While some suggested that the CAS phase was stable to about 44 GPa and 2000 K, others reported that the CAS phase decomposed into a mixture of Dvm, Crn, and St at around 30 GPa and 2000 K (49, 50). We observed CAS phase from 15 to 26 GPa, in good agreement with the decomposition report of CAS. At pressure and temperature above 42 GPa and 1300 K, a new phase was observed together with St + Dvm + Cr. From 42 to 49 GPa, the new phase was better observed after quench from heating. When compressed above 50 GPa and heated >1600 K, the same new peaks were still observed and developed profoundly during heating, suggesting a stable high-pressure phase. Based on above observations, we draw the boundary for this new phase assemblage around 42 GPa. As previously reported, St may undergo

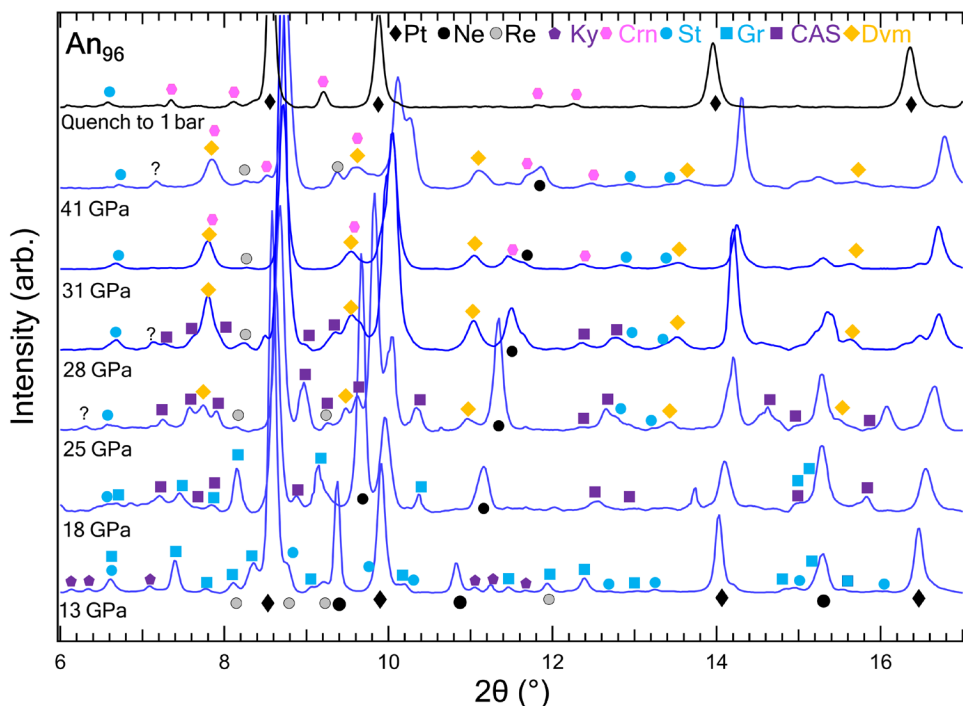


Fig. 3. High-pressure phase assemblages from decomposition of anorthite. Representative XRD patterns of anorthite (An₉₆) obtained at 13 to 41 GPa after quench from high temperatures. Only Crn and St were observed from the quenched pattern at ambient conditions. Different solid symbols denote different phases. Re, Rhenium; Ky, Kyanite.

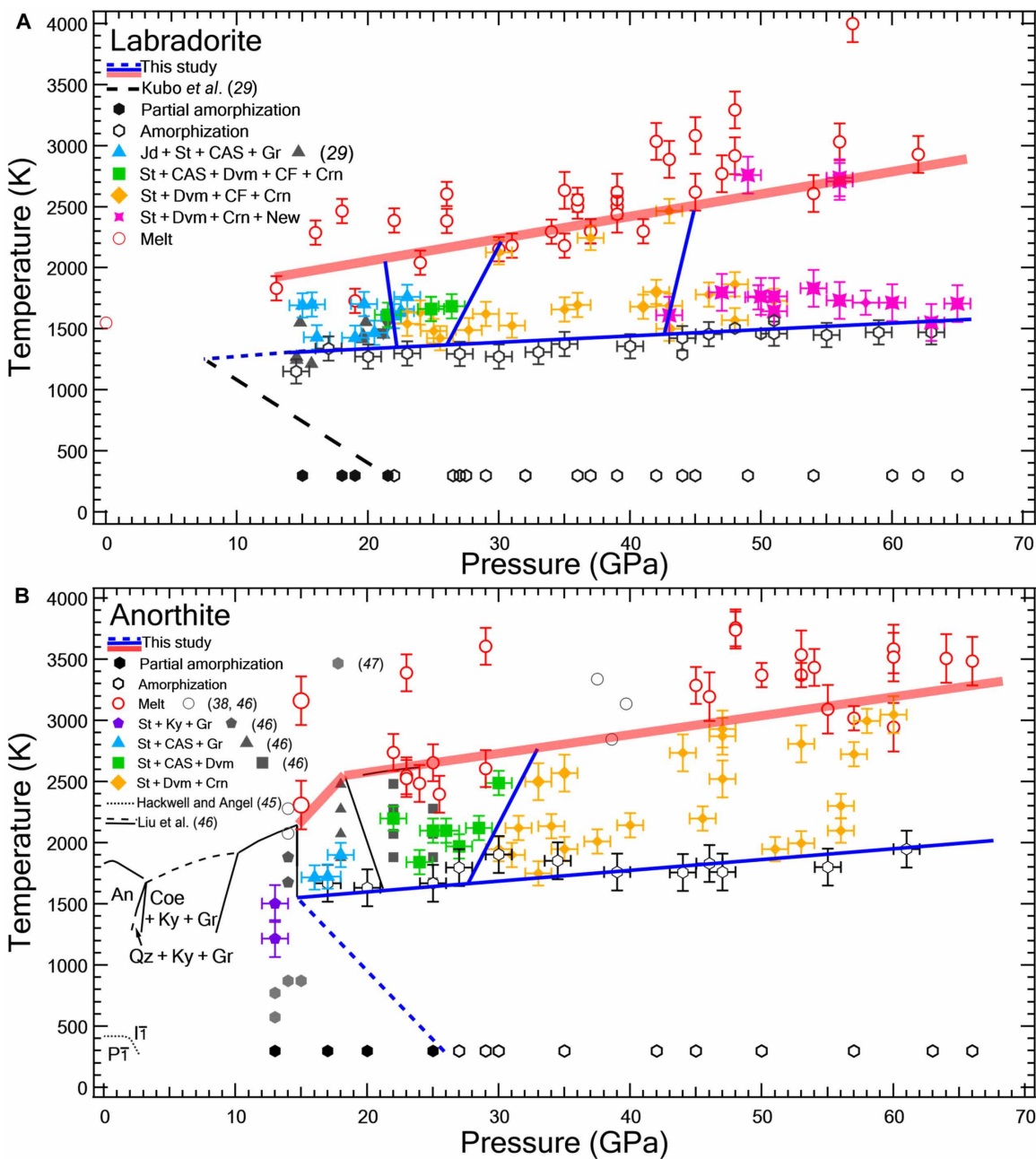


Fig. 4. Phase diagram of plagioclase. Phase diagram of labradorite An_{51} (A) and anorthite An_{96} (B). Solid/dashed blue and red lines are phase boundaries drawn from this study. The pressure and temperature error bars are also shown.

a displacive phase transition to the orthorhombic CaCl_2 -type SiO_2 phase at ~ 50 GPa (51). However, no CaCl_2 -type SiO_2 phase was observed in this study.

Similarly, when compressing anorthite An_{96} , we observed the gradual loss of the crystallinity from 13 to 25 GPa, indicated by the decreasing peaks in diffraction patterns. When compressed above 26 GPa, anorthite showed a complete loss of crystalline features at low temperatures (< 1400 K), this pressure range agrees with previous amorphization studies (27, 47, 52). Therefore, the crystalline to amorphization boundary of anorthite was drawn with negative slope similar to the amorphization boundary of labradorite An_{51} .

Also, moderate-temperature boundary around 1500 K was drawn between amorphous anorthite and its high-pressure phases. Note that crystal structure changes and phase boundaries below 22 GPa are adapted from Hackwell and Angel (45) and Liu *et al.* (46) (Fig. 4B). When compressed between 10 to 25 GPa, a phase boundary between $\text{St} + \text{Gr} + \text{Ky}$ and $\text{St} + \text{CAS} + \text{Gr}$ was determined by the disappearance of Ky, and later, the phase boundary between $\text{St} + \text{CAS} + \text{Gr}$ and $\text{St} + \text{CAS} + \text{Dvm}$ was determined mainly by the phase transition from Gr to Dvm. The boundary between $\text{St} + \text{CAS} + \text{Dvm}$ and $\text{St} + \text{Dvm} + \text{Crn}$ was determined by the disappearance of CAS above 30 GPa (50), similar to the one drawn for labradorite, but with a

slightly gentler slope. Compared to the one drawn for labradorite, this boundary shifts to higher pressures, possibly because of the chemical composition differences.

To induce melting at high pressure, high temperatures were reached by burst laser heating amorphous labradorite and anorthite with a duration of 0.1 to 0.3 s. During heating, the anomaly diffusion scattering hump shown around 8° to 9° in diffraction pattern were used as indication for melting (Fig. 5). After quench, the appearance of bull's eye patterns at the heating spots, a sign of thermal expansion, was also used as evidence for melting (Fig. 5). Melting line of labradorite was thus determined in the range of 15 to 65 GPa, extending from the melting point at ambient conditions from Bowens (Fig. 4A) (36). Melting line of anorthite was also determined in the similar pressure range but drawn at higher temperatures, extending from previous report by Liu *et al.* (46), and in good agreement with the shock melt data from Schmitt *et al.* (38) (Fig. 4B).

Formation of diaplectic glass and maskelynite

The colorless and optical isotropic appearance, chemical composition, morphology, and texture of diaplectic glass suggest that it is an amorphous plagioclase formed via solid-state transformation. Previous static compression experiments suggested the pressure for complete amorphization of plagioclase crystals is above 22 GPa at ambient temperature, and the pressure for amorphization will decrease as temperature increases (27–29). In Fig. 6, our phase diagram shows that labradorite will stay amorphous until heated above 1300 K, whereas for anorthite, the amorphization is below 1500 K. When combined with shock Hugoniot data from various plagioclase crystals and plagioclase-rich rocks (22, 24, 53, 54), our phase diagrams suggested diaplectic glass with intermediate plagioclase composition can be formed, under 42 GPa, 1450 K in basalt, 45 GPa, 1450 K for oligoclase crystals, and 57 GPa, 1550 K for granite. For Ca-rich plagioclase, anorthite crystals will turn into diaplectic glass below 47 GPa and 1800 K, 53 GPa and 1900 K for basalt, and 60 GPa

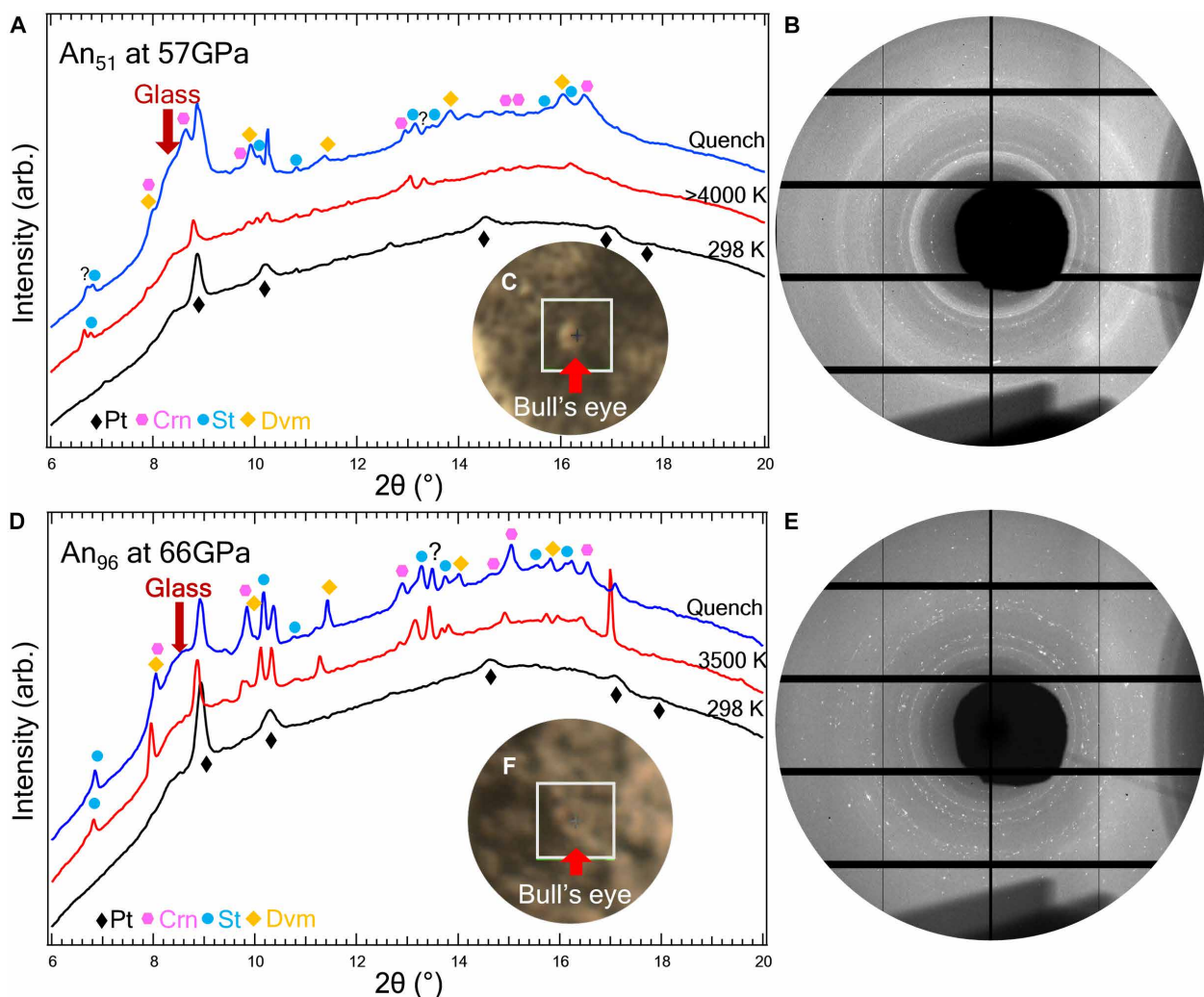


Fig. 5. Melting of labradorite An_{51} and anorthite An_{96} . (A and D) Diffraction patterns from one burst heating cycle of labradorite at 57 GPa and anorthite at 66 GPa, collected from preheating, during, and after heating; the diffusion scattering hump from glass in quench pattern is marked by the red arrow. (B and E) Two-dimensional (2D) diffraction images after heating from labradorite and anorthite, respectively. (C and F) Optical images after heating, showing the bull's eye in heating spot, marked by red arrow. The white square is 20 μm by 20 μm , and the cross marks the middle of the heating spot.

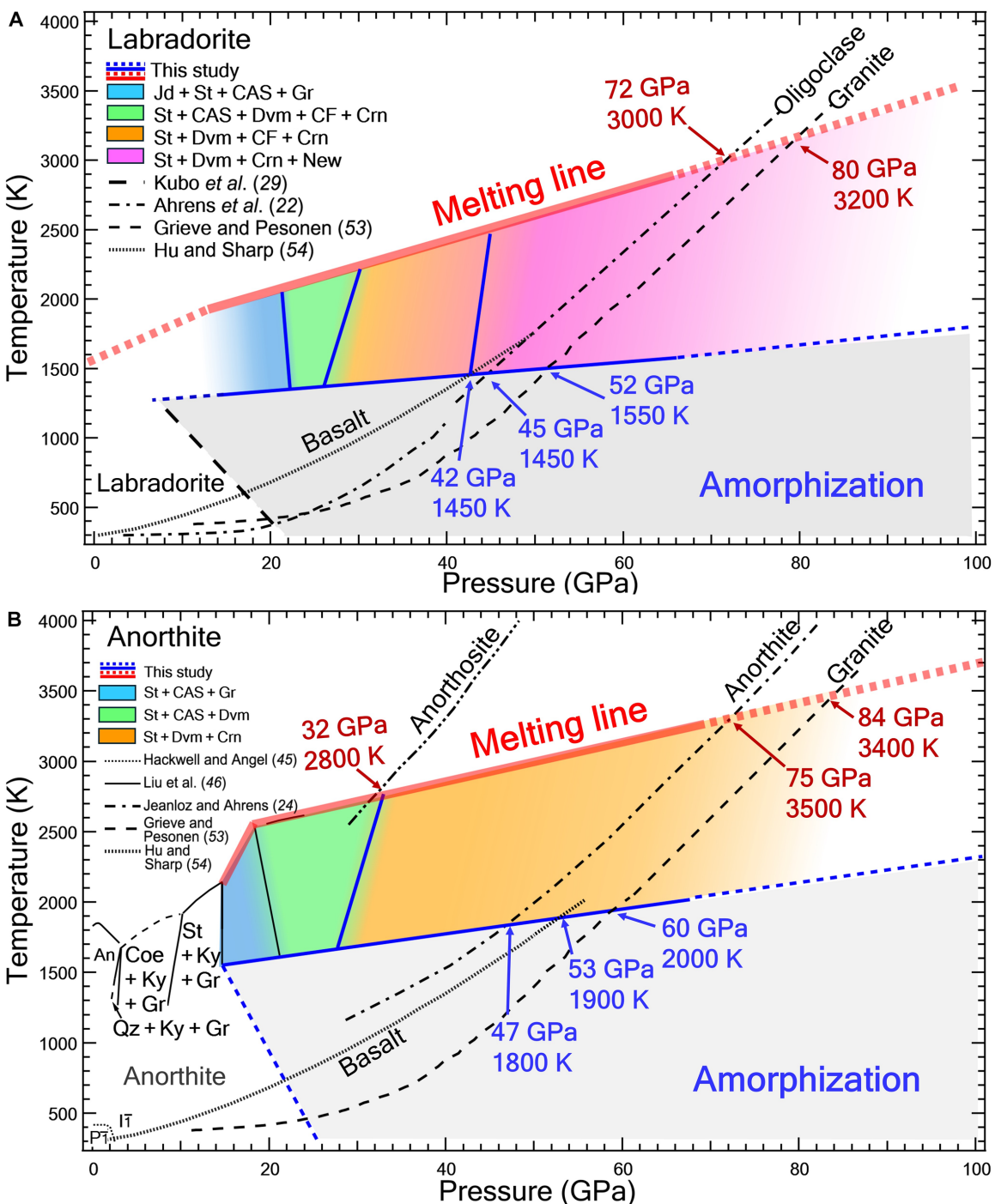


Fig. 6. The formation of dialektic glass and maskelynite. Phase diagram of labradorite An_{51} (A) and anorthite An_{96} (B), together with Hugoniot data from plagioclase (oligoclase $\text{Ab}_{75}\text{An}_{19}$ and anorthite An_{96}) and plagioclase-rich rocks [basalt and granite in both (A) and (B) and anorthosite with 19% porosity in (B)] (22, 24, 55, 57). Pressure and temperature conditions for amorphization (marked in blue) and melting (marked in red) are obtained from intersection of phase boundaries and Hugoniot curves of different minerals and rocks. Qz, Quartz; Coe, Coesite.

and 2000 K for granite. For porous anorthosite, diaplectic glass may be formed under much lower pressures and temperatures.

Maskelynite, while being colorless and isotropic similar to diaplectic glass, has some features that suggested that it is formed from plagioclase via a different path. Optically, maskelynite is smooth with no inherited texture from plagioclase but shown a nonvesicular flow pattern, in contrast with surrounding minerals bearing abundant radiated fractures, suggesting that it is formed from melting (8, 34, 35). Spectroscopically, while showing similar broad peaks around 500 and 1000 cm⁻¹ to diaplectic glass, Raman spectra from maskelynite shows distinguishably higher intensity of the peak around 1000 cm⁻¹ (16, 34, 55). This points to more nonbridging oxygens and short-range order characteristics in maskelynite than diaplectic glass (56), which can be attributed to higher temperature heating. Nevertheless, because of the limited understanding of the behavior of plagioclase under extended high-pressure temperature conditions, these differences between diaplectic glass and maskelynite have been overlooked, resulting in confusion and misinterpretation. In Fig. 6, we extrapolated the melting lines of plagioclase in our phase diagram to intersect with shock Hugoniot data. It is suggested that melting of oligoclase requires pressure and temperature to reach at least 72 GPa and 3000 K, and melting of labradorite in granite requires 80 GPa and 3200 K and 84 GPa and 3400 K for anorthite. Also, while anorthite can be melted above 75 GPa and 3500 K, it could also be melted only at 32 GPa and 2800 K in porous anorthosite, such as lunar highland rock with 19% porosity (24). Moreover, depending on the quench rate and melting paths, some high-pressure phases such as St and CAS can be observed next to maskelynite in meteorites (54, 57, 58). It is evident that our phase diagrams of labradorite and anorthite show invaluable information that can be combined with Hugoniot data collected from a wide range of plagioclase-bearing rocks for the investigation of hypervelocity impact events on terrestrial planetary bodies.

MATERIALS AND METHODS

Starting material

Natural intermediate plagioclase from Labrador, Canada and anorthite from Miyake-Jima, Tokyo, Japan were used as starting materials in this study. Intermediate plagioclase labradorite An₅₁ was selected as a starting material due to its composition similar as the shocked plagioclase from terrestrial impact craters and Martian meteorites, and anorthite An₉₆ was selected as a representative composition based on Apollo samples (16). The detailed chemical composition of labradorite and anorthite samples is listed in table S1. Their chemical compositions were analyzed by a JXA-8530F field emission electron probe microanalyzer at the University of Western Ontario. Quantitative chemical composition of the labradorite and anorthite crystals was determined with beam operating conditions at accelerating voltage of 10 to 15 kV, probe current of 20 nA, and a beam diameter of <5 μm. Mineral calibration standards used for wavelength dispersive spectrometry analyses were as follows: albite (CM Taylor) for Na and Si, Orthoclase (CM Taylor) for Si and K, and anorthite (Smithsonian USNM 137041, Great Sitkin Island, AL) for Al and Ca.

Labradorite An₅₁ and anorthite An₉₆ crystals were ground separately into powder (1 to 3 μm). A 10% platinum powder was mixed with each starting material, which served as a laser absorber and internal pressure standard. The sample mixtures were compressed into

a ~15- to 20-μm-thick disc and loaded in a 120- to 50-μm-diameter rhenium gasket sample chamber, which was pre-indented to a thickness of 30 to 35 μm. Small crumbles of sample were added on both sides of the disc to separate it from the diamond anvils. The elevation of the disc allows the pressure medium to flow above and below samples for maintaining the samples in a quasi-hydrostatic environment. Neon was loaded as a pressure medium and thermal insulation. One or two ruby spheres were used as the second pressure standard for gas loading. The gas loading was operated at GeoSoilEnviroCARS, Advanced Photon Source. Ruby pressures are determined by the ruby fluorescence method, and platinum pressure was determined by the equation of state of platinum (59). For melting plagioclase runs, amorphous silicon dioxide (SiO₂) was used as pressure medium and insulator.

In situ high-pressure room-temperature Raman experiment on single crystal

High-pressure and room-temperature single-crystal Raman study was performed on labradorite An₅₁ at the high-pressure diamond anvil cell laboratory, University of Western Ontario. The micro-Raman is a custom-built system equipped with a 514.5-nm laser and 500-mm focal length spectrometer. The beam size was focused by a 50× objective and estimated to have a spot size of about 2 μm. The laser power onto the sample is about 6 mW. The instrument control and data collection are performed by WinSpec software. The labradorite An₅₁ crystal was polished into a thin disk and loaded in T301 steel gasket sample chamber. A 4:1 mixture of methanol and ethanol was used as a pressure medium. Methanol + ethanol mixture provides nearly hydrostatic condition at ambient temperature up to its glass transition at 10 GPa (60). Two ruby spheres were loaded next to the labradorite An₅₁ disk as a pressure marker. The pressure was determined by ruby fluorescence method based on the shift of the R1 line (61).

In situ high-pressure and high-temperature synchrotron x-ray diffraction experiment

In situ high-pressure and high-temperature synchrotron x-ray diffraction (XRD) experiments were performed at beamline 13-ID-D of the GeoSoilEnviroCARS, sector of the Advanced Photon Source. Monochromatic x-ray beam with a wavelength of 0.3344 Å was focused to a beam size of 3 μm by 4 μm (62). LaB6 was used for sample-to-detector distance calibration. In situ synchrotron XRD images were collected before, during, and after heating at each pressure step. Thermal pressure during heating was determined by the equation of state of Pt (59). Errors of pressure were decided by averaging the calculated pressure from different diffraction peaks of Pt, usually within 1 GPa. Samples were heated by the double-sided laser-heating system with a yttrium lithium fluoride (YLF) fiber laser and a heating spot with ~20-μm diameter to achieve temperatures up to 4000 K, in either continuous or burst mode. Errors of temperature were determined by averaging the reading from both upstream and downstream, usually around 50 to 150 K. Continuous heating time varied from 30, 60, to 120 min due to the sluggish phase transition from amorphous plagioclase, while burst heating time varied from 0.1 to 3 s to gauge the melting temperature. The temperature of the heated spots was determined by fitting Planck equation to the thermal radiation spectra from both sides of the sample. The synchrotron x-ray diffraction images were collected by Pilatus 1 M CdTe 3X detector with exposure times of 0.1 to 30 s

during heating and after temperature quench. XRD mapping of the heated area was performed.

After decompression to 1 bar, some quenched products were examined at beamline 13-BM-C, sector of GSECARS, Advanced Photon Source. LaB6 was used for sample-to-detector distance calibration. The wavelength of the monochromatic x-ray beam at 13-BM-C was 0.434 Å, and beam size was focused to 12 μm by 18 μm. XRD patterns were collected by Pilatus 1 M Si detector, and the exposure time of each image was 90 to 120 s. Two-dimensional images of synchrotron XRD pattern were integrated and reduced to one-dimensional patterns using Dioptas software (63). Element mapping using EPMA was also performed on quenched samples to understand the element distributions at the University of Western Ontario. Because of the small size of the samples, they were not polished, and therefore, the concentration of the elements in the mapping results should be considered qualitative but not quantitative.

Supplementary Materials

This PDF file includes:

Figs. S1 and S2

Tables S1 and S2

References

REFERENCES AND NOTES

1. L. D. Ashwal, G. M. Bybee, Crustal evolution and the temporality of anorthosites. *Earth Sci. Rev.* **173**, 307–330 (2017).
2. L. D. Ashwal, Anorthosites, R. Asha, Ed. (Springer, Berlin, 1993).
3. W. L. Brown, I. Parsons, in *Feldspars and their Reactions*, I. Parsons, Ed. (Springer, 1994).
4. G. L. Hashimoto, M. Roos-Serote, S. Sugita, M. S. Gilmore, L. W. Kamp, R. W. Carlson, K. H. Baines, Felsic highland crust on Venus suggested by Galileo near-infrared mapping spectrometer data. *J. Geophys. Res.* **113**, E00B24 (2008).
5. B. Mason, Feldspar in chondrites. *Science* **148**, 943 (1965).
6. K. A. Milam, H. Y. McSween, J. Moersch, P. R. Christensen, Distribution and variation of plagioclase compositions on Mars. *J. Geophys. Res. Planets* **115**, 1–15 (2010).
7. A. L. Sprague, D. B. Nash, F. C. Witteborn, D. P. Cruikshank, Mercury's feldspar connection mid-IR measurements suggest plagioclase. *Adv. Space Res.* **19**, 1507–1510 (1997).
8. P. Gillet, A. El Goresy, Shock events in the solar system: The message from minerals in terrestrial planets and asteroids. *Annu. Rev. Earth Planet. Sci.* **41**, 257–285 (2013).
9. B. M. French, Traces of catastrophe, a handbook of shock-metamorphic effects in terrestrial meteorite impact structures (Lunar and Planetary Institute Houston, TX, 1998).
10. R. A. F. Grieve, G. R. Osinski, L. L. Tornabene, Planetary impacts, in *Encyclopedia of the Solar System* (Elsevier Inc., 2014).
11. A. E. Rubin, Maskelynite in asteroidal, lunar and planetary basaltic meteorites: An indicator of shock pressure during impact ejection from their parent bodies. *Icarus* **257**, 221–229 (2015).
12. D. Stöfpler, C. Hamann, K. Metzler, Shock metamorphism of planetary silicate rocks and sediments: Proposal for an updated classification system. *Meteorit. Planet. Sci.* **53**, 5–49 (2018).
13. W. von Engelhardt, J. Arndt, D. Stöffler, W. F. Müller, H. Jeziorkowski, R. A. Gubser, Diaplectische Glaser in den Breccien des Ries von Nördlingen als Anzeichen für Stosswellenmetamorphose. *Contrib. Mineral. Petrol.* **15**, 93–102 (1967) [Diaplectic glasses in the breccias of the Nördlingen Ries as evidence of shock-wave metamorphism].
14. W. von Engelhardt, D. Stöfpler, "Stages of shock metamorphism in crystalline rocks of the Ries basin, Germany," in *Shock Metamorphism of Natural Materials*, B. M. French, N. M. Short, Eds. (Mono Book Corp., 1968), pp. 159–168.
15. P. B. Robertson, R. A. F. Grieve, Impact structures in Canada—Their recognition and characteristics. *J. Roy. Astron. Soc. Can.* **69**, 1–21 (1975).
16. T. Xie, G. R. Osinski, S. R. Shieh, Raman study of shock features in plagioclase feldspar from the Mistastin Lake impact structure, Canada. *Meteorit. Planet. Sci.* **55**, 1471–1490 (2020).
17. W. von Engelhardt, J. Arndt, W. F. Müller, D. Stöffler, Shock metamorphism in lunar samples. *Science* **167**, 669–670 (1970).
18. N. M. Short, The nature of the Moon's surface: Evidence from shock metamorphism in Apollo 11 and 12 samples. *Icarus* **13**, 383–413 (1970).
19. S. J. Jaret, J. R. Johnson, M. Sims, N. DiFrancesco, T. D. Glotch, Micro spectroscopic and petrographic comparison of experimentally shocked albite, andesine, and bytownite. *J. Geophys. Res. Planets* **123**, 1701–1722 (2018).
20. J. Fritz, V. Assis Fernandes, A. Greshake, A. Holzwarth, U. Böttger, On the formation of diaplectic glass: Shock and thermal experiments with plagioclase of different chemical compositions. *Meteorit. Planet. Sci.* **54**, 1533–1547 (2019).
21. J. Hu, P. D. Asimow, Y. Liu, C. Ma, Shock-recovered maskelynite indicates low-pressure ejection of shergottites from Mars. *Sci. Adv.* **9**, eadf2906 (2023).
22. T. J. Ahrens, C. F. Petersen, J. T. Rosenberg, Shock compression of feldspars. *J. Geophys. Res.* **74**, 2727–2746 (1969).
23. R. V. Gibbons, T. J. Ahrens, Effects of shock pressures on calcic plagioclase. *Phys. Chem. Miner.* **1**, 95–107 (1977).
24. R. Jeanloz, T. J. Ahrens, Anorthite: Thermal equation of state to high pressures. *Geophys. J. Int.* **62**, 529–549 (1980).
25. R. Ostertag, Shock experiments on feldspar crystals. *J. Geophys. Res. Solid Earth* **88**, B364–B376 (1983).
26. D. J. Milton, P. S. De Carli, Maskelynite: Formation by explosive shock. *Science* **140**, 670–671 (1963).
27. Q. Williams, R. Jeanloz, Static amorphization of anorthite at 300 K and comparison with diaplectic glass. *Nature* **338**, 413–415 (1989).
28. N. Tomioka, H. Kondo, A. Kunikata, T. Nagai, Pressure-induced amorphization of albitic plagioclase in an externally heated diamond anvil cell. *Geophys. Res. Lett.* **37**, L21301 (2010).
29. T. Kubo, M. Kimura, T. Kato, M. Nishi, A. Tominaga, T. Kigekawa, K. Funakoshi, Plagioclase breakdown as an indicator for shock conditions of meteorites. *Nat. Geosci.* **3**, 41–45 (2010).
30. M. Sims, S. J. Jaret, E. Carl, B. Rhymer, N. Schrot, V. Mohrholz, J. Smith, Z. Konopkova, H.-P. Liermann, T. D. Glotch, L. Ehm, Pressure-induced amorphization in plagioclase feldspars: A time-resolved powder diffraction study during rapid compression. *Earth Planet. Sci. Lett.* **507**, 166–174 (2019).
31. G. Tschermak, Die Meteoriten von Shergotty und Gopalpur, in *Sitzungsbericht der Kaiserlichen Akademie der Wissenschaften* (Wien, K.-K. Hof- und Staatsdruckerei in Commission bei C. Gerold's Sohn; 1872), vol. 65, pp. 122–146 [The Shergotty and Gopalpur meteorites].
32. G. Tschermak, Beitrag zur Klassifikation der Meteoriten. *Sitzber. Akad. Wiss. Wien Math.-Naturwiss. Kl. Abt. I* **88**, 347–371 (1883) [Contribution to the classification of meteorites].
33. R. A. Binns, Stony Meteorites bearing Maskelynite. *Nature* **213**, 1111–1112 (1967).
34. M. Chen, A. El Goresy, The nature of maskelynite in shocked meteorites: Not diaplectic glass but a glass quenched from shock-induced dense melt at high pressures. *Earth Planet. Sci. Lett.* **179**, 489–502 (2000).
35. A. El Goresy, P. Gillet, M. Miyahara, E. Ohtani, S. Ozawa, P. Beck, G. Montagnac, Shock-induced deformation of Shergottites: Shock-pressure and perturbations of magmatic ages on Mars. *Geochim. Cosmochim. Acta* **101**, 233–262 (2013).
36. N. L. Bowen, The melting phenomena of the plagioclase feldspars. *Am. J. Sci.* **35**, 577–599 (1913).
37. T. J. Ahrens, J. D. O'Keefe, Shock melting and vaporization of lunar rocks and minerals. *Moon* **4**, 214–249 (1972).
38. D. R. Schmitt, T. J. Ahrens, Temperatures of shock-induced shear instabilities and their relationship to fusion curves. *Geophys. Res. Lett.* **10**, 1077–1080 (1983).
39. J. R. Goldsmith, The melting and breakdown reactions of anorthite at high pressures and temperatures. *Am. Mineral.* **65**, 272–284 (1980).
40. M. B. Boslough, T. J. Ahrens, A. C. Mitchell, Shock temperatures in anorthite glass. *Geophys. J. Int.* **84**, 475–489 (1986).
41. L.-G. Liu, High-pressure phase transformations of albite, jadeite and nepheline. *Earth Planet. Sci. Lett.* **37**, 438–444 (1978).
42. D. C. Presnall, Phase diagrams of earth-forming minerals, in *Mineral Physics and Crystallography: A Handbook of Physical Constants AGU Ref. Shelf*, T. J. Ahrens, Ed. (AGU, Washington, D.C., 1995), vol. 2, pp. 248–268.
43. X. Liu, Phase relations in the system $KAlSi_3O_8-NaAlSi_3O_8$ at high pressure-high temperature conditions and their implication to the petrogenesis of lingunite. *Earth Planet. Sci. Lett.* **246**, 317–325 (2006).
44. R. J. Angel, Order-disorder and the high-pressure P1-I1 transition in anorthite. *Am. Mineral.* **77**, 923–929 (1992).
45. T. P. Hackwell, R. J. Angel, Reversed brackets for the $P\bar{I} = I\bar{I}$ transition in anorthite at high pressures and temperatures. *Am. Mineral.* **80**, 239–246 (1995).
46. X. Liu, H. Ohfuji, N. Nishiyama, Q. He, T. Sanehira, T. Irifune, High-Pbehavior of anorthite composition and some phase relations of the $CaO-Al_2O_3-SiO_2$ system to the lower mantle of the Earth, and their geophysical implications. *J. Geophys. Res. Solid Earth* **117**, B09205 (2012).

47. A. Pakhomova, D. Simonova, I. Koemets, E. Koemets, G. Aprilis, M. Bykov, L. Gorelova, T. Fedotenko, V. Prakapenka, L. Dubrovinsky, Polymorphism of feldspars above 10 GPa. *Nat. Commun.* **11**, 2721 (2020).
48. T. Kubo, M. Kono, M. Imamura, T. Kato, S. Uehara, T. Kondo, Y. Higo, Y. Tange, T. Kikegawa, Formation of a metastable hollandite phase from amorphous plagioclase: A possible origin of lingunitite in shocked chondritic meteorites. *Phys. Earth Planet. In.* **272**, 50–57 (2017).
49. S. Ono, T. Iizuka, T. Kikegawa, Compressibility of the calcium aluminosilicate, CAS, phase to 44 GPa. *Phys. Earth Planet. In.* **150**, 331–338 (2005).
50. K. Ishibashi, K. Hirose, N. Sata, Y. Ohishi, Dissociation of CAS phase in the uppermost lower mantle. *Phys. Chem. Miner.* **35**, 197–200 (2008).
51. R. A. Fischer, A. J. Campbell, B. A. Chidester, D. M. Reaman, E. C. Thompson, J. S. Pigott, V. B. Prakapenka, J. S. Smith, Equations of state and phase boundary for stishovite and CaCl_2 -type SiO_2 . *Am. Mineral.* **103**, 792–802 (2018).
52. I. Daniel, P. Gillet, P. F. McMillan, G. H. Wolf, M. A. Verhelst, High-pressure behavior of anorthite: Compression and amorphization. *J. Geophys. Res.* **102**, 10313–10325 (1997).
53. R. A. F. Grieve, L. J. Pesonen, The terrestrial impact cratering record. *Tectonophysics* **216**, 1–30 (1992).
54. J. Hu, T. G. Sharp, Formation, preservation and extinction of high-pressure minerals in meteorites: temperature effects in shock metamorphism and shock classification. *Prog. Earth Planet Sci.* **9**, 6 (2022).
55. J. Fritz, A. Greshake, D. Stöffler, Micro-Raman spectroscopy of plagioclase and maskelynite in Martian meteorites: evidence of progressive shock metamorphism. *Antarct. Meteorite Res.* **18**, 96–116 (2005).
56. S. K. Sharma, B. Simons, H. S. Yoder, Raman study of anorthite, calcium Tschermak's pyroxene, and gehlenite in crystalline and glassy states. *Am. Mineral.* **68**, 1113–1125 (1983).
57. N. Tomioka, M. Miyahara, High-pressure minerals in shocked meteorites. *Meteorit. Planet. Sci.* **52**, 2017–2039 (2017).
58. O. Tschauner, C. Ma, Discovering high-pressure and high-temperature minerals, in *Celebrating the International Year of Mineralogy*, L. Bindu, G. Cruciani, Eds. (Springer, 2023).
59. Y. Fei, A. Ricolleau, M. Frank, K. Mibe, G. Shen, V. Prakapenka, Toward an internally consistent pressure scale. *Proc. Natl. Acad. Sci. U.S.A.* **104**, 9182–9186 (2007).
60. G. J. Piermarini, S. Block, J. D. Barnett, R. A. Forman, Calibration of the pressure dependence of the R_1 ruby fluorescence line to 195 kbar. *J. Appl. Phys.* **46**, 2774–2780 (1975).
61. H. K. Mao, J. Xu, P. M. Bell, Calibration of the ruby pressure gauge to 800 kbar under quasi-hydrostatic conditions. *J. Geophys. Res. Solid Earth* **91**, 4673–4676 (1986).
62. V. B. Prakapenka, A. Kubo, A. Kuznetsov, A. Laskin, O. Shkurikhin, P. Dera, M. L. Rivers, S. R. Sutton, Advanced flat top laser heating system for high pressure research at GSECARS: Application to the melting behavior of germanium. *High Press. Res.* **28**, 225–235 (2008).
63. C. Prescher, V. B. Prakapenka, DIOPTAS: A program for reduction of two-dimensional X-ray diffraction data and data exploration. *High Press. Res.* **35**, 223–230 (2015).
64. M. Akaogi, A. Tanaka, M. Kobayashi, N. Fukushima, T. Suzuki, High-pressure transformations in NaAlSiO_4 and thermodynamic properties of jadeite, nepheline, and calcium ferrite-type phase. *Phys. Earth Planet. In.* **130**, 49–58 (2002).
65. S. R. Shieh, T. S. Duffy, B. Li, Strength and elasticity of SiO_2 across the stishovite- CaCl_2 -type structural phase boundary. *Phys. Rev. Lett.* **89**, 255507 (2002).
66. S. Zhai, E. Ito, Phase relations of $\text{CaAl}_4\text{Si}_2\text{O}_{11}$ at high-pressure and high-temperature with implications for subducted continental crust into the deep mantle. *Phys. Earth Planet. In.* **167**, 161–167 (2008).
67. M. Akaogi, M. Haraguchi, K. Nakanishi, H. Ajiro, H. Kojitani, High-pressure phase relations in the system $\text{CaAl}_4\text{Si}_2\text{O}_{11}$ - $\text{NaAl}_3\text{Si}_3\text{O}_{11}$ with implication for Na-rich CAS phase in shocked Martian meteorites. *Earth Planet. Sci. Lett.* **289**, 503–508 (2010).
68. H. Chen, S.-H. Shim, K. Leinenweber, V. Prakapenka, Y. Meng, C. Prescher, Crystal structure of CaSiO_3 perovskite at 28–62 GPa and 300 K under quasi-hydrostatic stress conditions. *Am. Mineral.* **103**, 462–468 (2018).
69. A. Dewaele, M. Torrent, Equation of state of α - Al_2O_3 . *Phys. Rev. B* **88**, 64107 (2013).
70. S. Milani, R. J. Angel, L. Scandolo, M. L. Mazzucchelli, T. B. Ballaran, S. Klemme, M. C. Domeneghetti, R. Miletich, K. S. Scheidl, M. Derzsi, K. Tokár, M. Prencipe, M. Alvaro, F. Nestola, Thermo-elastic behavior of grossular garnet at high-pressure and temperatures. *Am. Mineral.* **102**, 851–859 (2017).
71. L. S. Dubrovinsky, N. A. Dubrovinskaya, V. B. Prokopenko, T. Le Bihan, Equation of state and crystal structure of NaAlSiO_4 with calcium-ferrite type structure in the conditions of the lower mantle. *High Press. Res.* **22**, 495–499 (2002).

Acknowledgments: This research used resources of the Advanced Photon Source, a US Department of Energy (DOE) Office of Science User Facility operated for the DOE Office of Science by Argonne National Laboratory under contract no. DE-AC02-06CH11357. We acknowledge the support of GeoSoilEnviroCARS (Sector 13), which is supported by the National Science Foundation–Earth Sciences (EAR-1634415). We are grateful for the help from beamline scientists and E. Greenberg with the use of the GSECARS beamline facility and GSECARS Raman Laboratory. We thank S. Tkachev for the use of GSECARS/COMPRES gas loading system. We thank J. Wang for helping with proposals and the usage of beamtime. T.X. thanks L. Ehm for the help with Crysfire2020. We thank the reviewers for their constructive comments. **Funding:** This work was supported by the Natural Sciences and Engineering Research Council of Canada (NSERC) RGPIN-2019-06818 (to S.R.S.) and the Natural Sciences and Engineering Research Council of Canada (NSERC) RGPIN-2024-05644 (to S.R.S.). **Author contributions:** Conceptualization: T.X. and S.R.S. Investigation: T.X., S.R.S., S.C., M.V.Z., R.D.R., V.B.P., and D.Z. Methodology: T.X., S.R.S., S.C., and D.Z. Resources: T.X., S.R.S., S.C., and M.V.Z. Data curation: T.X., S.R.S., M.V.Z., and D.Z. Formal analysis and software: T.X. Validation: T.X., S.R.S., and D.Z. Visualization: T.X. and S.R.S. Supervision: S.R.S. Funding acquisition: S.R.S. Project administration: S.R.S. and T.X. Writing—original draft: T.X. and S.R.S. Writing—review and editing: T.X., S.R.S., S.C., R.D.R., V.B.P., and D.Z. **Competing interests:** The authors declare that they have no competing interests. **Data and materials availability:** All data needed to evaluate the conclusions in the paper are present in the paper and/or the Supplementary Materials.

Submitted 8 January 2025

Accepted 16 May 2025

Published 20 June 2025

10.1126/sciadv.adv8231